Materials Advances

ROYAL SOCIETY OF CHEMISTRY

PAPER

View Article Online
View Journal

Cite this: DOI: 10.1039/d5ma01022e

Boosting the brightness of short-wave infrared emission in $YPO_4:Yb^{3+}/Er^{3+}$ phosphors: optimal photoluminescence quantum yield *versus* particle size

Krishnan Rajagopalan,*[a] Guojun Gao,[b] Lucas J. B. Erasmus,[c] Dmitry Busko,[a] Bryce S. Richards [ad] and Andrey Turshatov [*a]

The use of luminescent tracers in plastic recycling presents a novel application opportunity for classical phosphor materials, such as co-doped YPO_4. In this study, we report the optimization of the photoluminescence quantum yield (PLQY) of $YPO_4:Yb^{3+}/Er^{3+}$ phosphors *via* a flux-assisted solid-state synthesis approach. Upon excitation of Yb^{3+} ions at 940 or 980 nm, efficient energy transfer to Er^{3+} ions enables strong emission at 1540 nm, with a maximum PLQY of 78% achieved under optimized synthesis conditions. This performance was obtained by annealing the phosphor at 1100 °C for 12 h in the presence of LiCl flux. Notably, a reduced synthesis temperature of 1000 °C and a much shorter annealing time of 3 h still yielded a high PLQY (72%) when the flux was present. To demonstrate practical applicability, the phosphors were integrated into two model systems: (1) dispersion of 300 ppm phosphor in transparent silicone (emulating a bulk polymer), and (2) surface printing on polyethylene foil with a loading of 10 μg cm^{-2} (emulating a label). In both cases, the measured brightness was significantly lower than that of a commercial $Y_2O_2S:Yb^{3+}/Er^{3+}$ phosphor, despite its much lower PLQY of only 7%. This discrepancy was attributed to the non-optimal particle size distribution of the YPO_4 phosphor, which induced non-optimal scattering, absorption, and emission losses in both demonstrator matrices. After optimizing particle size *via* dry milling, the luminescence performance of the YPO_4-based phosphor surpassed that of the commercial reference in both configurations, confirming its suitability for use in luminescent tagging of plastics.

Received 7th September 2025,
Accepted 3rd December 2025

DOI: 10.1039/d5ma01022e

rsc.li/materials-advances

1. Introduction

The plastic packaging (PLP) industry is the largest consumer of plastics, using various types of thermoplastics such as polystyrene (PS), polyethylene terephthalate (PET), polypropylene (PPE), polyvinyl chloride (PVC), and polyethylene (PE).[1–3] The global thermoplastics production reached approximately 413 million metric tons in 2023 and is expected to increase to 450 to ~600 million metric tons between 2025 and 2050.[4,5] Within the European Union (EU), packaging consumes 40% of all plastics used; hence, member states must minimize the packaging waste per capita by at least 10% and 15% by 2030 and 2035, respectively (relative to 2018 levels).[6,7] According to EU regulation (2025/40), by January 2030, all PLP components that reach the market must contain a minimum percentage of recycled content, as determined by an average per manufacturing plant and year. For example, 30% of contact-sensitive packaging (for instance, food, pharmaceuticals, healthcare, or cosmetics products) must be made of recycled PET, with the exception of single-use plastic beverage bottles.[8] In addition to increasing CO_2 emissions, the expanding use of PLP poses significant challenges for recycling, particularly when the packaging's multilayer design prevents it from being collected separately.[6,7] This situation highlights the pressing need for implementing packaging regulations that support environmental conservation, and hence, immediate measures need to be taken to strengthen the circular economy.[9,10] As a first stage in the circular economy, qualitative collection and sorting of post-consumer plastic waste promotes the reduction of littering on a global scale.[11]

Although the existing recycling methods, such as chemical and mechanical recycling, and energy recovery methods, provide ways of handling plastic waste, they have limitations that

[a] Institute of Microstructure Technology, Karlsruhe Institute of Technology, Hermann-von-Helmholtz-Platz 1, 76344, Eggenstein-Leopoldshafen, Germany. E-mail: krishnan.rajagopalan@kit.edu, andrey.turshatov@kit.edu
[b] Polysecure GmbH, St. Georgener Str. 19, 79111, Freiburg, Germany
[c] Department of Physics, University of the Free State, Bloemfontein, 9300, South Africa
[d] Light Technology Institute, Karlsruhe Institute of Technology, Engesserstrasse 13, 76131 Karlsruhe, Germany

can hinder their effectiveness.[12] Mechanical recycling is not suitable for all types of plastics and faces challenges with contamination and the quality of recycled material. While chemical recycling may handle contaminated or a wider range of plastic types, it is energy-intensive, expensive, handles large volumes of waste, and may not be suitable for food-grade packaging materials.[13] The energy recovery (or thermal recycling) method utilizes plastic waste as a fuel source to produce heat or power, raising environmental problems over emissions and ash disposal.[14]

State-of-the-art industrial plastic waste near-infrared (NIR) sorting equipment is used prior to recycling. It employs InGaAs spectrometer to identify polymeric materials based on their reflectance spectra. This helps to distinguish the molecular structure of their polymer by measuring their reflectance spectra. A halogen lamp is used to irradiate the plastic waste, with the reflected light subsequently detected by an InGaAs sensor in the 1000–2000 nm range - commonly referred to as NIR range in the plastic-sorting processes, though more precisely classified as the shortwave infrared (SWIR) region.[15] However, despite being state-of-the-art, this technique struggles to accurately sort multiple types of plastic waste, particularly multilayer packaging, plastic films, complex packaging designs, and black plastics.[16] Advanced sorting technologies capable of achieving this differentiation to separate waste with more precise details are still developing. Therefore, urgent action is needed to address the critical challenge of recycling plastic waste by developing more accurate sorting technologies, preferably by enhancing existing NIR sorters, to enable better differentiation of various plastic types.

Tracer-based sorting (TBS) is a spectroscopic method of differentiating plastic waste, which uses a down-shifting (DS) or upconversion (UC) inorganic luminescent tracer (LT). The LT is typically a microcrystalline and chemically inert material that only emits light after being optically excited with NIR light (typically 940 or 980 nm), thus providing an identification code.[17] Both the UC emission (400–800 nm) or DS emission (1000–2000 nm) of the LT can be detected quickly above the background noise *via* a silicon or InGaAs detector, respectively.[18] Because the intensity of standard halogen lighting used in NIR sorting is insufficient to generate detectable luminescence from LT, alternative illumination is required. A compact NIR laser is therefore needed for optical excitation of LT. As the conveyor belt carrying the plastic waste moves at ~ 3 m s^{-1}, the InGaAs sensor records the plastics' reflectance $R < 100\%$, whereas LT's emission is observed by a signal $R > 100\%$. The diagrammatic representation of the NIR sorting process with the installation of a 980 nm laser is shown in Fig. 1(a). If plastic containing LT is identified as part of the rejected fraction, precision-controlled air nozzles will release pressurised air to expel the plastic waste. The main advantage is that the LT can be printed or labelled on its packaging cover without directly integrating it into the plastic, as illustrated in Fig. 1(b). Using LT with printing ink is highly effective for incorporating them into the packaging cover. Printed LT on the packaging cover can be removed before recycling to prevent the tracer from being carried over upon plastic recycling.[18] Unlike other prints or surface structuring, the TBS eliminates the need to position the package with respect to the detecting unit because the LT's emission is isotropic and emits signals in all directions, enabling $\approx$100% waste identification.[18,19] As the LT typically requires parts-per-million (ppm) level, one representative example (Y_2O_2S:Ln^{3+}) has been approved for use in food contact products and medical devices after passing all relevant tests, including toxicological tests.[20]

The TBS process employs LTs based on trivalent lanthanide (Ln^{3+}) ions – such as Yb^{3+} (sensitizer), along with Ho^{3+}, Er^{3+}, and Tm^{3+} (activator) – to achieve distinctive emission spectrum characteristics (due to the Ln^{3+} f–f electronic transitions) that cover the SWIR spectral range. Yb^{3+} has relatively strong and broad absorption between 940–980 nm and has a broad emission peak centred at about 1000 nm. In addition, if Yb^{3+} is co-doped with one of the Ho^{3+}, Er^{3+}, and Tm^{3+} ions, then SWIR emission at around 1200 nm, 1540 nm, and 1800 nm (extended InGaAs spectral range) can be achieved, respectively. The Ln^{3+} SWIR emission is relatively unaffected by PLP and provides a background-free signal (see Fig. 1(a)). Among the Ln^{3+} ions, Er^{3+} ions are the focus of the current work because they undergo a large emission cross-section due to the $^4I_{13/2} \rightarrow {}^4I_{15/2}$ intra-4f transition.[22] Furthermore, the LT must exhibit high PLQYs and strong absorption cross-sections, allowing concentrations in the ppm range to be sufficient. Currently available commercial LT (Y_2O_2S:Yb^{3+},Er^{3+}) has a DS PLQY of around 7%. Therefore, developing Er^3-based LT materials with a high PLQY is essential.

Among different host matrices, tetragonal YPO_4 (I41/amd) features several intriguing characteristics, notably an easy synthesis procedure, good luminescence PLQY, non-hygroscopic, thermally and chemically resilient, and low toxicity.[23–27] More importantly, YPO_4 is reported as a potentially strong contender for SWIR emission when doped with Yb^{3+}/Er^{3+}.[27–29] A recent study showed that Yb^{3+} and Er^{3+} doped YPO_4 emitting SWIR luminescence at 1540 nm could produce a remarkable 67% PLQY.[27] Thus, it is beneficial to continue researching YPO_4:Yb^{3+}/Er^{3+} phosphor to further improve its SWIR emission properties.

In many instances, YPO_4:Yb^{3+}/Er^{3+} is synthesized using a conventional solid-state reaction (SSR) method.[24,25,27] However, some of the characteristics of SSR, such as the high annealing temperature ($\geq$1200 °C), along with the need for several days of annealing time, multiple heating cycles, and intermediate grinding, are disadvantages and require optimisation. Additionally, SSR often produces particles with a poorly controlled size distribution, which is critical for optical performance. This process can yield particles ranging from sub-micron dimensions to several hundred micrometres. Table S1 in the SI highlights the limitations of the SSR conditions reported in the literature, including the multiple steps involved in synthesising YPO_4, as demonstrated in previous works.

Adding flux to SSR can help to overcome the aforementioned limitations while enhancing luminescence simultaneously. This is achieved by improving the size and morphology of the

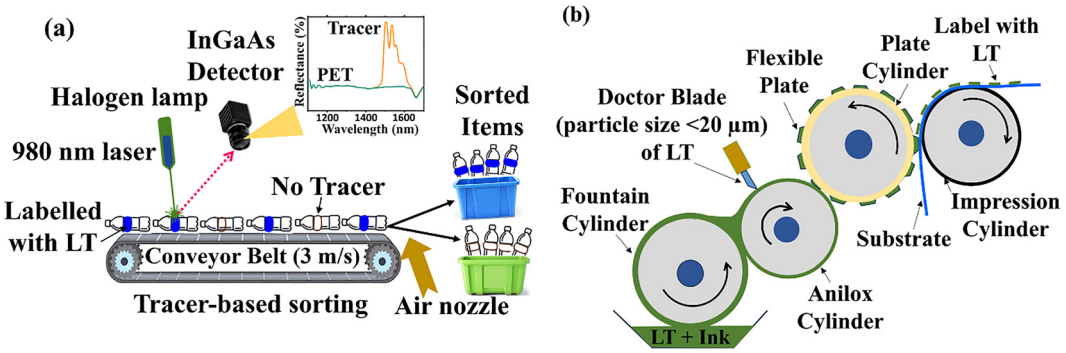

Fig. 1 (a) illustrates the TBS process with the installation of a 980 nm laser within a standard NIR sorting machine. As the plastic items pass by at 3 m s^{-1}, detectors on the conveyor belts identify LT's signal within a few milliseconds. If the LT emits in the visible/NIR range, the same sensor head can simultaneously detect hyperspectral imaging of both the tracers' signal and the plastics' polymer type using SWIR InGaAs line-scan. The InGaAs detector is set up to pick out the brightest peak, and the air nozzle will be triggered to expel the plastic by blowing pressurized air on it. For example, polyethyleterephthalate (PET) items with LT can be easily separated. (b) schematically demonstrates the typical relief printing process used to print LT particles on the substrate (normally on a packaging material). It uses flexible plates to print an ink mixture (ink + LT particles) onto the surface being printed. Water-based or solvent-based inks are used, depending on the substrate and desired properties.[21]

particles, increasing the diffusion coefficient of the components, and facilitating the incorporation of dopant ions. Well-known flux compounds – such as BaF_2, NaF, LiF, NaCl, LiCl, and Li_2CO_3 – could potentially reduce the SSR reaction temperature and annealing time, as demonstrated by previous research.[30–33] Of all the flux materials, LiCl has been extensively utilized and proven to enhance the optical characteristics.[34–36]

In the present work, the use of LiCl as a flux is proposed to lower the SSR temperature, annealing time, minimise the number of heating cycles, and reduce the intermediate grinding steps to enhance luminescence output. Furthermore, this study addresses the key research question of how adding LiCl flux facilitates the enhancement of PLQY in the SWIR emission of YPO_4:Yb^{3+},Er^{3+} phosphors. To this end, the relationship between the PLQY at 1540 nm and key synthesis parameters is systematically investigated, including annealing temperature, duration, and LiCl flux concentration. The optimization of PLQY was combined with another critical challenge of the SSR method: that of achieving an optimal particle size distribution.

It was earlier hypothesized that for achieving the strongest luminescent brightness, LTs with particle sizes in the range of a few micrometers (1–10 μm) are more effective than larger (>10 μm) particles due to their favourable optical scattering.[27] Hereafter, a dimensionless parameter brightness (B) is defined as the product of the fraction of absorbed light (A) and the PLQY:

$$B = A \times \mathrm{PLQY} = (1 - e^{N\sigma L}) \times \mathrm{PLQY} \quad (1)$$

where: N – number of optical centers per cm^3; σ – absorption cross-section, cm^2; L – optical pathlength.

It should be noted that brightness can have different definitions in the literature, depending on the intended application of the luminescent material.[37] In practice B is often difficult to determine directly because accurate measurements of A or PLQY can be experimentally challenging. In such cases, it is convenient to discuss the brightness enhancement (ΔB) between two samples, (i) and (j):

$$\Delta B = \frac{B_i}{B_j} = \frac{(1 - e^{-N_i\sigma_i L_i}) \times \mathrm{PLQY}_i}{(1 - e^{-N_j\sigma_j L_j}) \times \mathrm{PLQY}_j} = \frac{F_i I_i}{F_j I_j} \quad (2)$$

where: F – instrumental factor related to the geometry of the sample and the parameters of the luminescence detection setup (typically $F_i = F_j$ for identical experimental conditions), and I – measured luminescence intensity.

This forms the basis for the second research question: how do PLQY and particle size affect the brightness of LTs when they are (i) incorporated at a concentration of 300 ppm into a layer of transparent silicone resin that is 2 mm thick and (ii) printed onto a flexible polypropylene film at concentration of 10 μg cm^{-2} using flexographic printing? (see Fig. 1(b))

2. Experimental section

2.1. LiCl-mediated SSR synthesis of YPO_4:Yb^{3+}/Er^{3+} phosphors

2.2.1. Materials. The raw ingredients used in this synthesis are Y_2O_3 (99.9%), Yb_2O_3 (99.9%), Er_2O_3 (99.9%), and $(NH_4)_2HPO_4$ (98%), which were purchased from ChemPur chemicals. LiCl (99.9%) is acquired from BLD Pharma Tech GmbH. All starting materials were used as received, without being purified further.

2.2.2. Synthesis. YPO_4:Yb^{3+}/Er^{3+} phosphors were synthesized using the SSR technique with and without LiCl flux at various annealing temperatures. Recent findings on the SSR approach have optimized the doping concentrations of Yb(24%) and Er(3%) in YPO_4,[27] and this concentration was fixed throughout all experiments. The starting materials with the appropriate molar ratio were mixed and ground uniformly for approximately 30 min using a mortar and pestle to achieve homogeneous mixtures.

2.2.3. Two-step SSR annealing. Homogeneously mixed ingredients were then transferred into an alumina crucible covered with a lid, pre-heated to 300 °C for 6 h (step-1). Followed by grinding and subsequently annealed to various annealing temperatures (900, 1000, 1100, 1200 °C) with a 5 °C min^{-1} heating rate for 12 h without and with the addition of LiCl flux (hereafter referred to as step-2).

2.2.4. One-step SSR annealing. The starting mixtures were directly annealed to various temperatures (900, 1000, 1100, 1200 °C) with a 5 °C min^{-1} heating rate for 12 h with the addition of LiCl flux.

After the samples reached room temperature, they were extracted from the furnace and manually ground into fine powders, which were then used for different characterizations.

2.2.5. Milling. Milling experiments were carried out using a planetary ball mill (Pulverisette-7, Fritsch, Germany). The milling was carried out using a dry-milling approach. The mass ratio of the material to milling balls was maintained at 1 : 10. Zirconia balls with a diameter of 5 mm (each weighing approximately 0.4 g) were used as the milling media, with a total of 25 balls placed in a 20 mL zirconia grinding bowl. All milling steps were conducted under dry conditions to prevent contamination and unwanted phase transformations. To find the optimum milling conditions, variables such as milling time and revolutions per minute (rpm) were investigated.

A series of SSR experiments was performed to achieve the highest PLQY by optimizing the number of heating cycles (one-step and two-step), annealing temperature, annealing time, and LiCl flux concentration as primary tasks.

2.2. Fabrication of model systems

To fabricate the polydimethylsiloxane (PDMS) film, 2-component silicones with a 1 : 1 ratio (Silicone Addition Clear 25 (Medium Hard), siliconeandmore, Netherlands) and LT powder with a concentration of 300 ppm were weighed and thoroughly mixed. The mixture was placed in a vacuum desiccator to remove entrapped air bubbles, poured into a steel mold with a dimension of 80 × 40 × 2 mm, and then cured on a hotplate at 120 °C for 15 min.

To fabricate the printed samples, LTs were applied to the surface of polyethylene (PE) foil using a printing process carried out by Siegwerk Druckfarben AG & Co. KGaA with an Erichsen GmbH & Co. KG Printing Proofer. In this method, ink containing the luminescent tracer is introduced into engraved cells on a printing plate. A doctor blade ensures that the ink remains within the engravings by removing any excess ink from the surface. The ink is then transferred to the substrate when a roller presses the engraved plate against it. Following deposition, the solvent is removed through forced air drying. The efficiency of ink transfer is governed by parameters such as engraving depth, roller pressure, and printing speed.

2.3. Structural and optical characterization

Powder X-ray diffraction (PXRD) using a Bruker-D2 phaser model coupled with Cu-K_α (1.5405 Å) radiation source facilitates the identification of the YPO_4 materials' crystal structures in the 2θ range 10–70° with a step size of 0.010° per second. The FullProf suite package was installed to perform Rietveld structural refinement to observe the changes in the lattice parameter, whereas the VESTA program[38] was utilized to visualize the YPO_4 crystal structure.

The produced particles' microscopic morphology and size were examined using a scanning electron microscope (SEM) (Zeiss, SUPRA 60VP). A small layer of silver, ~10 nm thick, was sputtered onto the samples to facilitate SEM imaging. A laser particle size analyzer (Analysette 22 NeXT Nano, Fritsch GmbH, Germany) was used to determine the particle size distribution (measurement range 0.01 to 3800 μm). Q3 (cumulative) and dQ3 (differential) in the graph correspond to particle size distribution, denoting the cumulative % of particles (by volume) and differential % of particles within a small size interval (by volume), respectively.

To determine the elemental composition in the synthesized samples, inductively coupled plasma optical emission spectroscopic (ICP-OES) analyses were performed using a iCAP 7600 DUO (Thermo-Fisher-Scientific) equipped with an Echelle grating optical system combined with a dual-segmented SCD detector.

The diffuse reflectance spectra (DRS) of the samples were measured using an Agilent Cary 7000 UV/Vis/NIR spectrophotometer equipped with an integrating sphere.

An optical setup constructed around an integrating sphere (Labsphere, Ø 6″, 3P-LPM-060-SL) was utilized to get the PLQY measurement. After positioning the sample in the center of the integrating sphere, a 940 nm (0.1 W cm^{-2}) continuous-wave laser diode (Thorlabs, M9-940-0200) was used to excite the synthesized sample. A laser diode controller (Thorlabs, ITC4001) was used to operate the laser diodes, which were mounted on a temperature-controlled mount (Thorlabs, TCLDM9). An NIR spectrometer (Ocean Insight, NIRQuest) was used to record the 1540 nm emission of Er^{3+} ($^4I_{13/2} \rightarrow {}^4I_{15/2}$) and the incident laser (940 nm). A 980 nm long-pass filter (Semrock, LP02-980RE-25) was inserted between the output terminal of the integrating sphere and the optical fiber's collecting point to minimize the excitation wavelength's intensity during the emission measurement. The PLQY was determined by employing the 3 M procedure. A silicon photodiode power sensor (Thorlabs, S121C) was illuminated by a portion of the laser beam reflected by a quartz wedge with a reflectivity of ~4%. A power meter (Thorlabs, PM320E) measured the excitation laser's output. The entire system was programmed and managed by in-house developers utilizing the LabVIEW platform.[39,40] A relative error of 3% was assumed for all measurements based on a previous publication, in which the repeatability of the results was assessed in detail.[27]

The decay time measurements were obtained using an in-house optical system built with an infrared single-photon detector (ID Quantique, ID220) attached to the multi-channel scaling card (TimeHarp 260, Picoquant).

The temperature-dependent luminescence properties were investigated utilizing a custom-built setup equipped with a high-performance temperature control stage (Microptik BV, MTDC600), functioning within a temperature range of 83–875 K. The sample

was exposed to irradiation with a 940 nm laser (Thorlabs, M9-940-0200) and was heated at a rate of 0.5 K s^{-1}, and its luminescence was measured using an NIR spectrometer (Ocean Insight, NIRQuest).

The model systems were characterized using excitation with 980 nm laser (Thorlabs, L980P200) with intensity of 10 W cm^{-2} and detection of luminescence with the NIR spectrometer (Ocean Insight, NIRQuest). Five arbitrary points on each sample were measured to calculate the average value of luminescence intensity.

It should be noted that two excitation wavelengths, 940 nm and 980 nm, are used in this study. Both wavelengths excite the same Yb^{3+}:$^2F_{5/2}$ state, but different Stark sublevels. The choice of excitation wavelength (940 nm *vs.* 980 nm) does not affect PLQY or lifetime values. The selection is mainly a matter of experimental convenience. Using a 940 nm laser simplifies the rejection of scattered light and allows integration of the full Yb^{3+} emission spectrum for accurate PLQY estimation. However, for practical demonstrations, the 980 nm laser is typically used because Yb^{3+} exhibits stronger absorption at this wavelength. For clarity, the following text explicitly specifies whether 940 nm or 980 nm excitation is applied.

2.4. Optical modelling

The simulation was done using LightTools software by Synopsys (see detailed description in SI)

3. Results and discussion

3.1. Optimization of annealing temperature in two-step SSR annealing of YPO_4:Yb^{3+},Er^{3+} without flux

Recent findings on YPO_4 material doped with 24% Yb^{3+} and 3% Er^{3+}, synthesized using the SSR without any flux addition, have achieved a maximum of 67% PLQY for the SWIR emission at $\approx$1540 nm (transition from $^4I_{13/2}$ to the $^4I_{15/2}$ state of Er^{3+}).[27] To reach maximum PLQY, the sample was preheated at 200 °C/3 h (step-1), followed by three repeating cycles of grinding and annealing at 1200 °C/12 h (step-2). Thus, the synthesis procedure required multiple heating cycles, a prolonged time (3 h + 36 h) with intermediate grinding (4 times) to reach the highest PLQY (67%). To reduce the duration of the annealing time, annealing temperature, and multiple grinding steps, herein both a two and a one-step SSR process were investigated using a low-melting LiCl as a flux to focus on further improving the PLQY.

To begin with, the step-2 SSR synthesis temperature was optimized, using a fixed 12 h annealing time, to obtain phase-pure YPO_4:Yb^{3+}/Er^{3+} material without any flux. Fig. 2a presents an overview of the PXRD data for YPO_4:Yb^{3+}/Er^{3+} samples preheated at 300 °C for 6 h (step-1) and annealed to various step-2 annealing temperatures (900 to 1300 °C) with a fixed 12 h annealing time.

When the step-2 annealing temperature was maintained at 900 °C and 1000 °C, the PXRD patterns consisted of many reflections belonging to the secondary phase marked with (*), indicating that the obtained crystal phase is not pure. However, as the temperature increased from 1100 to 1300 °C, the impurity phase disappeared, indicating the formation of a phase-pure material. The resulting PXRD patterns closely match those of phase-pure YPO_4 previously reported in the literature[24,25,27,41] and correspond to the tetragonal phase of YPO_4 with the zircon structure, characterized by the space group *I*41/*amd*. A relatively minor shift in position toward high angle, compared to the undoped YPO_4 sample, is observed due to the doping effect of Yb/Er^{3+} in the Y^{3+} site in YPO_4.

In the zircon-structured YPO_4, Y^{3+}/Yb^{3+}/Er^{3+} atoms are connected to eight O^{2-} atoms in an 8 coordination symmetry, and P^{5+} is attached to four identical O^{2-} atoms in a tetrahedral geometry. Fig. 2b depicts the Rietveld structural refinement technique applied to the XRD data of the YPO_4: 24%Yb^{3+},3%Er^{3+} sample annealed at 1200 °C, to examine the structural parameters of the YPO_4 crystal lattice. The refined unit cell parameters are furnished in Table S2.

The representative DRS measured in the range 950–1650 nm for the sample annealed at 1200 °C (step-2) temperature is shown in Fig. 2c. The DRS spectrum consists of absorptions at 980 nm and 1540 nm due to the $^2F_{5/2}$ state of Yb^{3+} ions and the $^4I_{13/2}$ state of Er^{3+} ions, respectively. During optical excitation of Yb^{3+} ions, the emission spectra of all the YPO_4:Yb^{3+}/Er^{3+} phosphor synthesized at various step-2 annealing temperatures show similar emission characteristics. The emission spectrum of the YPO_4:Yb^{3+}/Er^{3+} synthesized at 1200 °C step-2 annealing temperature, presented in Fig. 2c, consists of a broad emission band starting from 1460 to 1650 nm, peaking at 1540 nm, which is attributed to the $^4I_{13/2} \rightarrow {}^4I_{15/2}$ transitions in the Er^{3+} ion. The other transition at shorter wavelengths, due to the Yb^{3+} ($^2F_{5/2} \rightarrow {}^2F_{7/2}$), is significantly weaker than the $^4I_{13/2} \rightarrow {}^4I_{15/2}$.

PLQY was evaluated for all the samples to ascertain the optimum temperature for the step-2 annealing process without any flux addition. Fig. 2d displays the PLQY results for powder samples synthesized at different step-2 temperatures (900, 1000, 1100, 1200, and 1300 °C, respectively). The measurements were taken under 940 nm excitation at 0.1 W cm^{-2} using an integrating sphere. When the step-2 annealing temperature of the SSR was kept at 900 °C and 1000 °C, the PLQY value was found to be ~7% and ~13%, respectively. As the step-2 annealing temperature increases to 1100 °C and 1200 °C, the PLQY correspondingly rises to 40% and 52%, respectively. However, upon further increasing the temperature to 1300 °C, the PLQY decreases slightly to 47%. These values remain significantly lower than the previously reported PLQY of 67%, achieved *via* a multi-cycle synthesis approach. This suggests that, although phase purity is attained under the present conditions, it does not guarantee sufficient interdiffusion and homogeneous mixing of Yb^{3+} and Er^{3+} ions necessary to achieve high PLQY.

The representative histogram in Fig. 2e shows the polymodal particle size distribution of the YPO_4:Yb^{3+}/Er^{3+} sample synthesized at 1200 °C temperature, indicating the presence of several populations of particle sizes (mean particle size ~26.3 μm) with the overall particle size range from 1 to 100 μm.

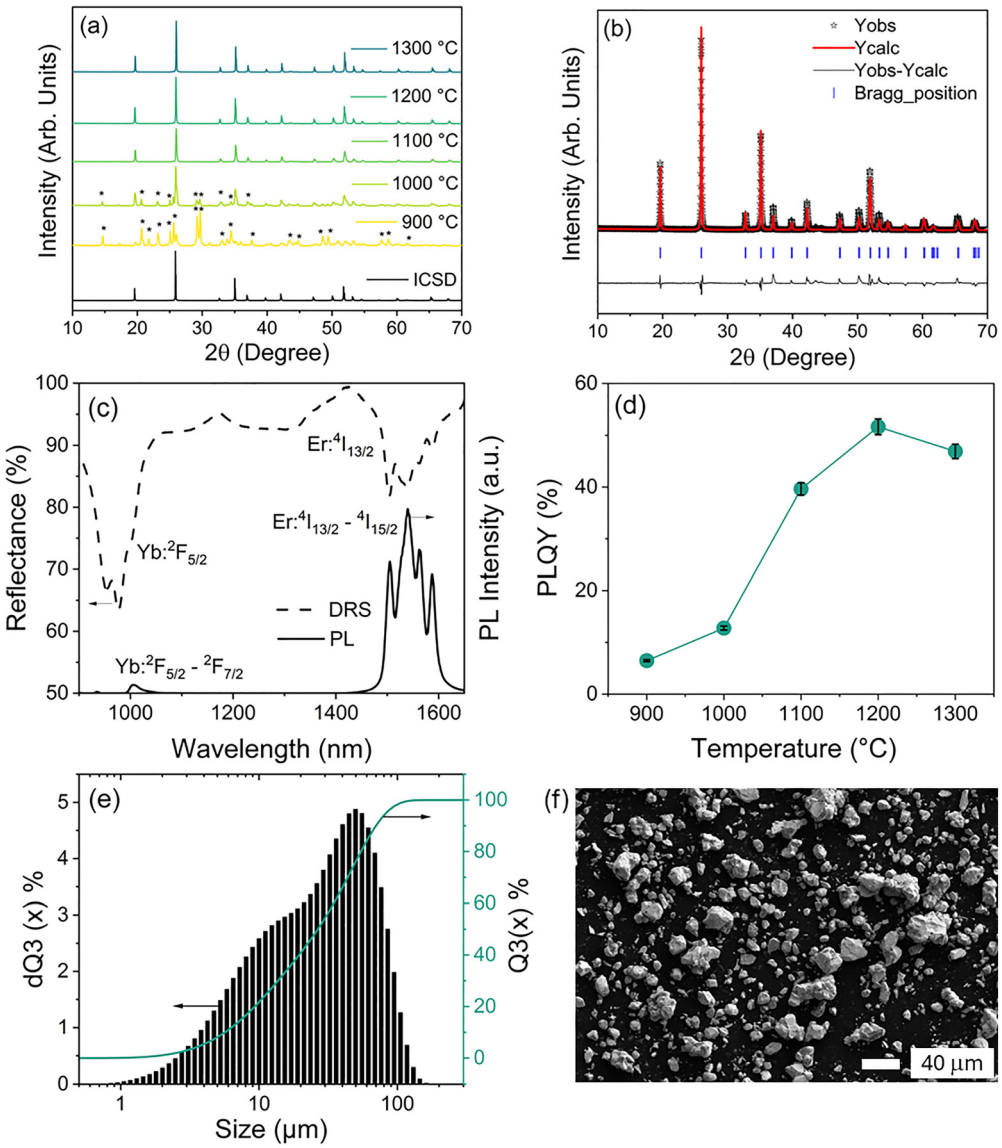

Fig. 2 (a) PXRD patterns of YPO_4:Yb^{3+}/Er^{3+} material annealed at different step-2 temperatures (900–1300 °C) for 12 h, synthesized using SSR without flux addition, ICSD – 117962. (b) representative Rietveld refinement of the sample synthesized at 1200 °C (c) DRS and PL emission spectrum of the YPO_4:Yb^{3+}/Er^{3+} sample synthesized annealed a 1200 °C, (d) PLQY of Er^{3+} emission (integrated over 1450–1650 nm) *vs.* step-2 annealing temperature under the 940 nm excitation, (e) representative particle size distribution histogram of the sample annealed at 1200 °C, and (f) corresponding SEM image.

Importantly, it was observed that as the step-2 temperature increases from 900 °C to 1300 °C, resulting in a greater number of particles moving towards a larger size range (see Fig. S1(a–d)). Further, image analysis using SEM, shown in Fig. 2f, confirms the existence of small and agglomerated microcrystalline clusters with polygonal morphology having a non-uniform size distribution. The grain boundaries between some aggregated particles are easily visible in some regions.

3.2. Optimization of temperature and LiCl flux concentration in two-step SSR annealing of YPO_4:Yb^{3+}/Er^{3+}

To enhance the PLQY, various concentrations of LiCl flux (ranging from 2% to 10%) were added, and the YPO_4:Yb^{3+}/Er^{3+} material was annealed at different step-2 temperatures for a fixed duration of 12 h. The step-1 preheating procedure remained unchanged. Fig. 3a shows the PXRD patterns of YPO_4:Yb^{3+}/Er^{3+}samples synthesized with various LiCl flux concentrations, annealed at 900 °C temperature for 12 h. It is observed that the addition of even 2% LiCl for the synthesis of YPO_4:Yb^{3+}/Er^{3+} material, the powder XRD patterns do not contain any impurity phase compared with those synthesized without LiCl flux. As the LiCl flux concentration increases from 2% to 10%, all the XRD patterns exhibit the pure phase, and these results are consistent with the standard data of the YPO_4 tetragonal phase. A minor shift in position toward high angle is noticed, similar to the case observed for the samples annealed at different step-2 temperatures without LiCl addition. Furthermore, the PXRD patterns of all YPO_4:Yb^{3+}/Er^{3+} material annealed

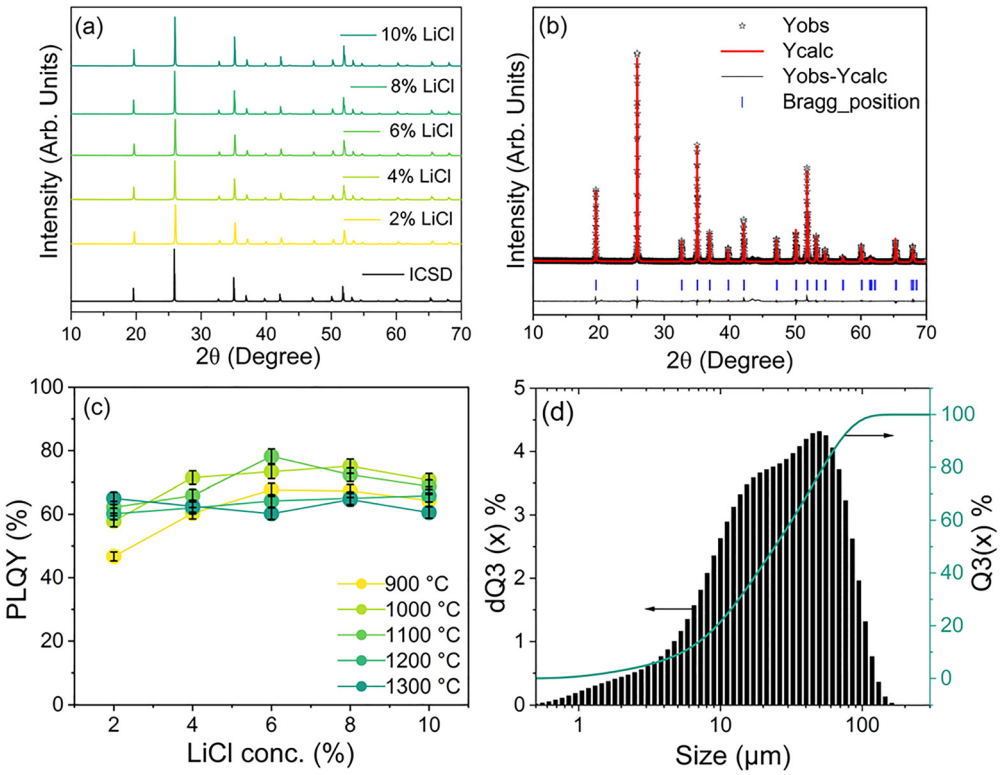

Fig. 3 (a) Powder XRD patterns of YPO_4:Yb^{3+}/Er^{3+} phosphor synthesized with different LiCl flux concentrations at 900 °C/12 h step-2 annealing process. ICSD – 117962. (b) Representative Rietveld refinement of the sample with addition of 6% LiCl flux and annealed at 1100 °C step-2 temperature, (c) PLQY (under the 940 nm excitation) of YPO_4:Yb^{3+}/Er^{3+} phosphors synthesized with various LiCl flux concentration *vs.* various step-2 annealing temperature with a fixed 12 h annealing time, (d) representative particle size distribution histogram of YPO_4:Yb^{3+}/Er^{3+} sample synthesized with 6% LiCl flux conc. and annealed at 1100 °C step-2 annealing temperature.

at various step-2 temperatures (1000, 1100, 1200, and 1300 °C) with the presence of LiCl (2, 4, 6, 8, 10%) display similar patterns. (see Fig. S2(a–d)).

Fig. 3b represents the Rietveld refinement analysis carried out for the representative sample synthesized with 6% LiCl flux and annealed at 1100 °C temperature. The refined crystallographic parameters are presented in Table S3, suggesting no significant changes were observed in the lattice parameters. It reveals that adding LiCl does not affect the crystal structure of the YPO_4 material. ICP-OES analysis is also performed to determine the elemental composition of the YPO_4:Yb^{3+}/Er^{3+} material to evaluate any influence of LiCl after annealing the sample. These results, presented in Table S4, suggest that most of the LiCl flux is lost - likely through evaporation - during the step-2 annealing of YPO_4:Yb^{3+}/Er^{3+} material. Only trace amounts of lithium were detected, with mass percentages of 0.07% and 0.06% for samples treated with 2% and 10% LiCl flux, respectively.

The effect of varying LiCl concentrations on the PLQY of YPO_4:Yb^{3+}/Er^{3+} material annealed at various step-2 temperatures was examined. The measurements were taken under 940 nm excitation at 0.1 W cm^{-2} using an integrating sphere. Fig. 3(c) shows the PLQY measured for the samples synthesized with various LiCl flux concentrations (2, 4, 6, 8, and 10%), annealed at various step-2 temperatures (900 to 1300 °C). The PLQY values peak at 76% and 78% for samples annealed at 1000 °C and 1100 °C, corresponding to 8% and 6% LiCl flux concentrations, respectively. These values are significantly higher than those obtained in the synthesis without the addition of a flux.

It is reasonable to attribute the observed high PLQY values to efficient energy transfer from Yb^{3+} to Er^{3+} ions. To evaluate the effectiveness of this energy transfer following the addition of LiCl as a flux, photoluminescence decay time measurements were performed. For this purpose, the best-performing sample - YPO_4:Yb^{3+}/Er^{3+} synthesized with LiCl flux and annealed at 1100 °C - was selected for decay profile analysis. The decay behavior was then compared to that of a reference YPO_4: Yb^{3+} sample synthesized under identical conditions, but without Er^{3+} doping. (Fig. S3). The YPO_4:Yb^{3+} sample exhibits a decay time of 2.3 ms when excited at 940 nm and monitored at approximately 1000 nm. Notably, this decay time is almost double that of the sample synthesised without LiCl flux (1.2 ms), as detailed in a previous study.[27] The decay time decreases to 0.35 ms after co-doping with Er^{3+} in YPO_4:Yb^{3+}. This confirms energy transfer from the populated $^2F_{5/2}$ state of Yb^{3+} to the $^4I_{13/2}$ state of Er^{3+} with an efficiency of 85%. Thus, it is likely that the addition of flux promotes Yb^{3+} and Er^{3+} intermixing compared to the no-flux synthesis, which exhibits an energy transfer efficiency of only 56%.[27] In our previous

work,[27] we established a correlation between cation intermixing, characterized by cathodoluminescence, and PLQY. We observed that when Yb^{3+} and Er^{3+} cations were poorly intermixed (after calcination for less than 60 hours at 1200 °C), the PLQY of the Er^{3+}:$^4I_{13/2}$ emission at 1540 nm was higher under Yb^{3+} (980 nm) excitation than under direct Er^{3+} (1510 nm) excitation. Conversely, when Yb^{3+} and Er^{3+} cations became well intermixed (after calcination at 1200 °C for 60 hours), this trend reversed: the PLQY under 980 nm excitation became lower than under 1510 nm excitation. Fig. S4 shows the PLQY of samples calcined at different temperatures without LiCl, as well as the sample calcined at 1100 °C with LiCl, under both 980 nm and 1510 nm excitation. The data clearly indicate that efficient cation intermixing occurs only in the presence of the LiCl flux, as only under this condition is the PLQY under 1510 nm excitation higher than under 980 nm excitation.

Further, Fig. S5 shows the intensity-dependent PLQY of the YPO_4:Yb^{3+}/Er^{3+} phosphors synthesized at 1100 °C (step-2) in the presence of various flux concentrations. The data in Fig. S5 confirms that the PLQY is highest, even when the excitation power is only 0.1 W cm^{-2}. However, the PLQY is slightly lower at higher excitation intensities.[42] Interestingly, the potential for further enhancement of PLQY can be inferred from the temperature-dependent luminescence measurements (Fig. S6). In this experiment, the sample exhibiting the highest PLQY of 78% was heated in the temperature range of 30–200 °C, and the steady-state luminescence intensity was recorded. As shown in Fig. S5, the luminescence intensity increases with temperature, reaching a value 1.1 times higher at 150 °C compared to that at 30 °C. Considering that the absorption cross-section of Yb^{3+} at 940 nm is expected to decrease slightly with increasing temperature due to peak broadening, this enhancement in luminescence intensity may correspond to a potential increase in PLQY to approximately 86% (78% × 1.1). This enhancement is most likely associated with more efficient energy transfer from Yb^{3+} to Er^{3+} at elevated temperatures. As the temperature rises, higher-energy Stark sublevels within the Yb^{3+}:$^2F_{5/2}$ manifold become thermally populated. This increases the driving force for downhill transfer to the Er^{3+}:$^4I_{13/2}$ state and suppress energy back-transfer, thereby improving transfer efficiency and boosting the overall luminescence output.

In addition to clearly enhancing the luminescent properties of the material, the incorporation of LiCl flux significantly influences the particle size distribution. Specifically, the addition of LiCl induces a transition from a broad monomodal distribution (Fig. S7(a)) to a polymodal distribution (Fig. S7(b–d), and Fig. 3d). This effect is attributed to the flux-promoted particle growth, which reduces the population of finer particles and shifts the overall distribution toward larger particle sizes. When the LiCl concentration was 8%, the particle size distribution in the larger size region decreased. When the LiCl concentration reached 10%, it the formation of more particles in the smaller size range was observed, in addition to the larger size range. Interestingly, this trend correlates with the slight decrease in PLQY observed for samples synthesised with 8% and 10% LiCl.

To further investigate the role of lithium-based fluxes, Li_2CO_3 was evaluated as an alternative to LiCl in the SSR synthesis at various step-2 annealing temperatures (Fig. S8). However, no significant improvement in PLQY was observed compared to the no-flux condition. This limited effectiveness is likely due to the thermal behavior of Li_2CO_3, which decomposes at 732 °C[43] into Li_2O and CO_2. The resulting Li_2O, with a high melting point of 1438 °C, does not exhibit a strong fluxing effect within the applied temperature range (900–1300 °C). In contrast, LiCl, with a lower melting point (~605 °C) and vaporization temperature (~1360 °C), forms a stable molten phase under the synthesis conditions. This liquid medium promotes enhanced particle interaction, sintering, and diffusion, thereby contributing to improved luminescent performance.[44]

3.3. Optimization of annealing time in two-step and one-step SSR annealing of YPO_4:Yb^{3+}/Er^{3+} in the presence of LiCl flux

The presence of LiCl flux was found to significantly enhance the PLQY, reaching up to 78% in the two-step SSR process, as compared to samples synthesized without LiCl addition (see Sections 3.2 and 3.1). In addition, efforts were made to reduce the annealing time and eliminate one annealing cycle by employing LiCl as a flux in a simplified one-step process.

A series of one-step SSR experiments was conducted at reduced annealing durations (3, 6, 9, and 12 h) and various temperatures (900, 1000, and 1100 °C) in the presence of LiCl flux. The absolute PLQY of each sample was assessed and compared to that obtained from the two-step synthesis. The YPO_4:Yb^{3+}/Er^{3+} compositions were synthesized under these conditions, and the corresponding PXRD data are provided in Fig. S9 and S10.

Fig. 4a presents the PLQY values of YPO_4:Yb^{3+}/Er^{3+} samples synthesized *via* a two-step SSR process using LiCl as a flux, with varying annealing times and temperatures. It should be noted that the highest PLQY at 900 °C was obtained using 8% LiCl, whereas a lower flux concentration of 6% was employed for all other temperatures. At 900 °C, the PLQY decreases moderately from 77% to 72% as the annealing time is reduced from 12 to 3 h, with a relatively high value of 73% still achieved after only 3 h of annealing. A comparable trend is observed at 1000 °C, where the PLQY decreases slightly from 78% to 75% as the annealing duration is shortened. In contrast, at 1100 °C, the PLQY remains nearly constant at approximately 78%, regardless of whether the annealing time is 3 or 12 h.

These results demonstrate that the addition of LiCl flux substantially enhances the reaction kinetics of the SSR process, allowing for the formation of highly luminescent materials even at reduced annealing times.

Fig. 4b displays the PLQY values of samples synthesized with LiCl flux and annealed at various temperatures (900, 1000, and 1100 °C) using a one-step SSR process, plotted as a function of annealing time. Based on the PXRD results, it is evident that the use of LiCl flux facilitates the formation of phase-pure YPO_4:Yb^{3+}/Er^{3+} even with an annealing time as short as 30 minutes at 900 °C, also in the one-step SSR process. As the annealing time decreases from 12 to 3 h, a slight reduction in

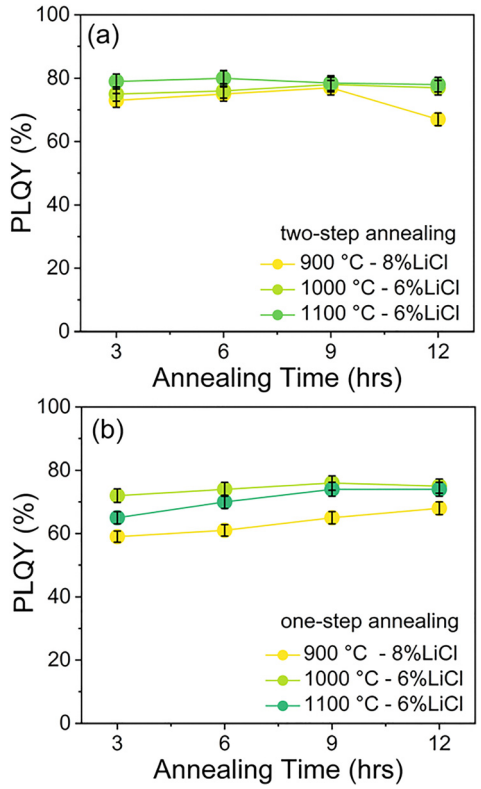

Fig. 4 Dependence of PLQY (under the 940 nm excitation) of 1540 nm emission in YPO_4:Yb^{3+}/Er^{3+} synthesized at different annealing times as a function of (a) two-step, (b) one-step synthesis using LiCl flux.

PLQY is observed. Notably, the values obtained at 1000 °C are mostly comparable to the maximum PLQY of 78%, achieved *via* the two-step SSR process at 1100 °C for 12 h.

These findings demonstrate the potential for significantly reducing both the number of heating cycles and the overall annealing duration in the SSR method when using LiCl flux, without substantial loss in PLQY. This is particularly relevant for large-scale gram-level synthesis, where optimizing annealing temperature and duration is critical for improving cost-effectiveness and process efficiency.

3.4. Control of particle size *via* optimization of milling conditions

The PLQY values reported in Sections 3.1–3.3 represent internal quantum yields, which quantify the ratio of emitted to absorbed photons. This metric reflects the efficiency of the target radiative transition relative to competing radiative and non-radiative pathways within the material. However, internal PLQY does not account for how efficiently the material absorbs excitation light, nor does it consider light scattering within the sample. Light scattering plays a crucial role in determining the effective photon residence time and path length within a material. This is particularly important, as photons may either be lost through backscattering before absorption or, conversely, undergo multiple scattering events that enhance the likelihood of absorption. Therefore, the perceived brightness of a luminescent material in real-world applications is governed by a complex interplay of absorption efficiency, scattering behavior, and internal PLQY.

To evaluate the practical brightness of YPO_4-based LTs, two representative application scenarios were examined: (1) bulk dispersion: the LT was embedded in a PDMS matrix at a relatively low concentration of 300 ppm by weight (Fig. 5a); (2) surface printing: the LT was incorporated into a printable ink formulation at 3 wt% and deposited *via* flexographic printing, resulting in a thin film with a high surface loading of approximately 10 μg cm^{-2} (Fig. 5b). To assess the real-world luminescence performance, the emission intensities of the YPO_4:Yb^{3+}/Er^{3+} (YPO) LT were compared with a commercially available reference material - Y_2O_2S:Yb^{3+}/Er^{3+} (YOS) LT - under identical experimental conditions.

Fig. 5c presents a counterintuitive observation: despite the relatively low internal PLQY of the reference YOS sample (7%), the luminescence intensity of the PDMS film containing YOS (batch#1) appears significantly stronger than that of the corresponding film containing YPO (batch#2), which exhibits a much higher internal PLQY of 78%. Similarly, for the printed samples (Fig. 5d), the YPO-based LT (batch#2) exhibits markedly lower luminescence intensity compared to the YOS-based printed film (batch#1).

This discrepancy can be attributed not only to differences in PLQY but also to disparities in particle size distribution between the two materials. As shown in Fig. S11 the YOS particles display a relatively narrow size distribution centered around ~4 μm, while the YPO particles exhibit a much broader size range, spanning from 1 to 100 μm (Fig. 3d). It is likely that light scattering effects play a significant role in these observations. Particles in the low-micrometer range scatter light more effectively within the polymer matrix (example of Mie scattering). This increases the optical path length and raises the probability of photon absorption. In contrast, the larger particles in the YPO sample produce weaker scattering (example of geometrical optics) and lower excitation efficiency, especially in low-concentration bulk composites such as PDMS films. To better understand this effect, we performed optical simulations using ray-tracing rendering software. The results (Fig. S12a, b, and Table S5) show that smaller particles, such as YOS markers, produce stronger light scattering and result in a higher number of luminescent photons reaching the detector that is in agreement with the experimental results (Fig. 5c).

Furthermore, due to the wider particle size distribution, the printing process (flexography) did not necessarily print all LT particles (>20 μm).[45] The engraved cells' depth in a doctor-blade system is generally 20 μm in a flexography printing technique (see Fig. 1b). This indicates that particles having a size greater than 20 μm will most likely be eliminated by the doctor blade system.

These results emphasize the importance of optimizing not only the luminescent efficiency but also the particle morphology and size distribution of phosphor materials for application-specific brightness performance. To enhance the brightness of YPO-based LTs and produce fine powders with particle sizes

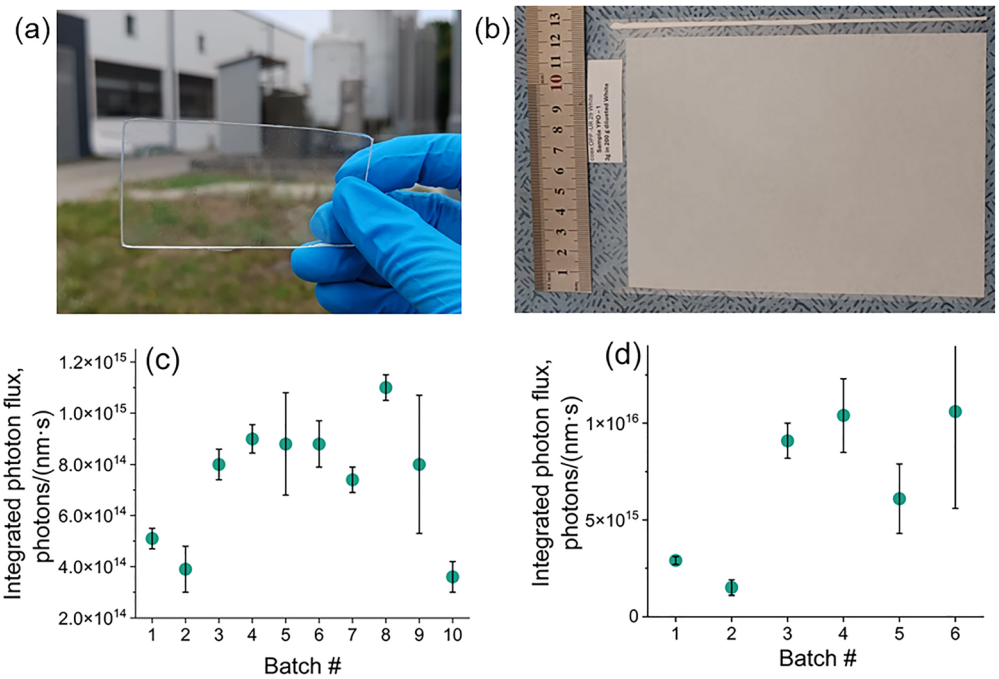

Fig. 5 (a) example of PDMS film with 300 ppm concentration of YPO LT; (b) example of printed sample with YPO LT; (c) luminescence intensity of the PDMS films with different LTs (300 ppm concentration): #1 – YOS reference sample, #2 – YPO unmilled sample, #3-#7 - YPO samples milled at constant 200 rpm and variable time of 5, 10, 20, 30, and 45 minutes, respectively, #8-#10 - YPO samples milled at constant time of 45 min and variable rpm of 230, 260 and 290 rpm, respectively; (d) luminescence intensity of the LTs printed on surface of polyethylene foil (surface concentration of 10 μg cm^{-2}): #1 – YOS reference sample, #2 – YPO unmilled sample, #3-#6 - YPO samples milled at constant time of 45 min and variable rpm of 200, 230, 260 and 290 rpm, respectively. The error bars in (c) and (d) were calculated based on measurements taken at five arbitrary points on the surface of the PDMS films and the printed sheets. Excitation wavelength 980 nm. Excitation intensity 10 W cm^{-2}.

below 20 μm, mechanical milling was employed to reduce bulk agglomeration and improve particle homogeneity. A systematic study was conducted to correlate PLQY with particle size distribution in order to identify optimal milling conditions by varying both milling time and rotational speed.

As shown in the particle size distribution histograms in Fig. 6a–e, even short milling durations (*e.g.*, 5 minutes) led to a significant shift in particle size distribution relative to the unmilled sample (Fig. 3d). At a constant milling speed of 200 rpm, the mean particle size decreased substantially from 9.5 μm (unmilled) to 3.4 μm after 45 minutes of milling, with all milled samples exhibiting a more uniform size distribution. Increasing the milling speed from 200 to 290 rpm further reduced the mean particle size to approximately 2.2 μm (Fig. S13).

However, despite achieving the desired particle size range, milling was found to have a pronounced negative impact on PLQY (Fig. 6f). A 5-minute milling duration resulted in a PLQY reduction to 51%, which further decreased to 30% after 45 minutes. The decline in luminescence efficiency is likely caused by the formation of microstructural, surface-related defects[46,47] *via* formation of microcracks or surface chemical reactions, that act as nonradiative recombination centers and quench the SWIR emission. High-energy milling induces lattice strain and generates broken or cracked particles, as evidenced by the broadening of Raman peaks (Fig. S14) and the SEM images (Fig. S15). According to the previous reports,[48,49] it is evident that the milling process clearly reduces particle size and induces particle fracture. Furthermore, freshly created surfaces are chemically active and can readily react with ambient moisture or CO_2, forming surface quenching centers such as OH or carbonate groups, as indicated by the FTIR spectra (Fig. S16). Overall, both the primary reduction in particle size and the secondary formation of surface-related defects enhance nonradiative recombination processes, resulting in a decrease in PLQY after milling.

Although the PLQY decreased, milling was found to significantly enhance the luminescence intensity of YPO-based LTs, as shown in Fig. 5c. In the PDMS film, YPO sample #8, milled for 45 minutes at 230 rpm, showed higher brightness than the commercial YOS LT. It should be emphasized that the particle-size dependence of luminescence intensity in PDMS films can be explained by light-scattering and light-absorption processes, which together determine excitation efficiency and light out-coupling. Milling produces smaller particles with a larger surface-to-volume ratio, increasing surface defects and non-radiative centers and thereby reducing PLQY. However, simulation results (Fig. S12 and Tables S5, S6) indicate a substantial increase in scattering and in the number of detected luminescence photons when milled YPO-based LT is used, consistent with the experimental results (Fig. 5c). Overall, these findings suggest that an optimal particle-size range exists in which surface defect

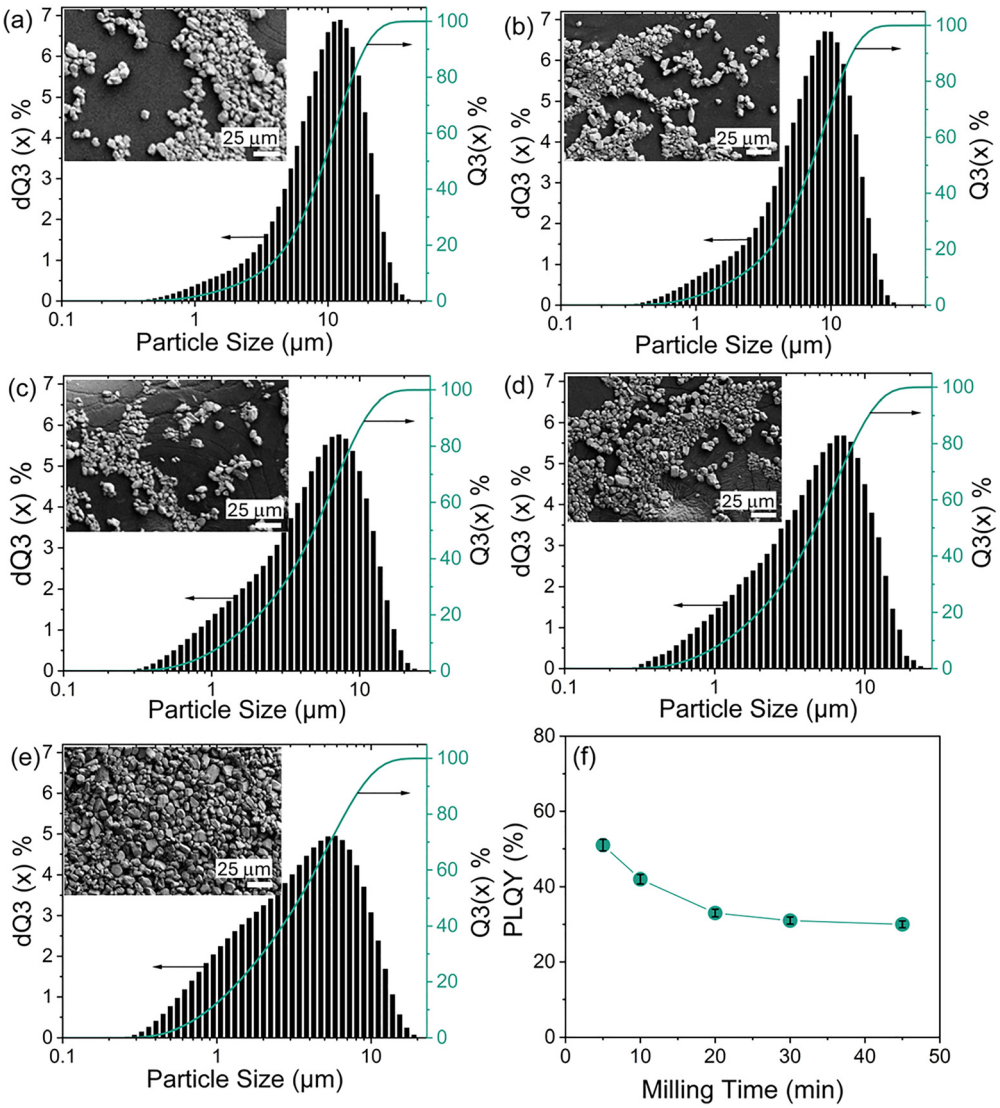

Fig. 6 Particle size distribution of samples synthesized at 1100 °C/12 h step-2 annealing procedure and milled with a fixed 200 rpm at various periods (a) 5 min, (b) 10 min, (c) 20 min, (d) 30 min, (e) 45 min, respectively. (f) milling time vs PLQY.

density is minimized and scattering is sufficiently enhanced, leading to maximum photoluminescence intensity.

Interestingly, a subsequent annealing step at relatively low temperatures (150–200 °C) following milling resulted in a partial recovery of the PLQY (Fig. S17), likely due to structural relaxation or the healing of defect states introduced during the milling process.

Furthermore, the optimised YPO LT (Fig. 5d, batch #5, milled 45 min at 230 rpm) much stronger outperformed the YOS-based reference in terms of luminescence intensity for the printed samples. This can be attributed to the high local concentration of LT in the thin printed luminescent layer, where PLQY is the main factor influencing luminescence intensity, and scattering plays a comparatively less critical role. There are also fewer particles lost during flexographic printing (Fig. 1b), since almost all particles are smaller than the depth of the engraved cells (20 μm).

4. Discussion

It has been demonstrated that LTs, including those exhibiting both Stokes and upconversion luminescence, can be effectively utilized for the labelling of PLP.[27] In addition to enabling NIR-based sorting of primary polymer types, LTs offer the potential for sub-classification of plastics with identical chemical compositions but differing specifications - such as food-grade *vs.* non-food-grade materials, packaging from different brands, or multilayer composite structures.

To realize this potential, it is desirable to develop a palette of LTs with spectrally distinguishable luminescence signatures for integration into state-of-the-art NIR sorting systems, with only a minimal system upgrade - specifically, the incorporation of a 940 or 980 nm excitation laser (Fig. 1a). In this context, the current work explores the Yb^{3+}/Er^{3+} ion pair as one promising LT candidate.

Several critical criteria must be considered when evaluating a luminescent material for use as an LT:

(1) High brightness: high luminescence brightness is essential to ensure reliable detection. Importantly, it is not necessary to incorporate the LT into the bulk polymer matrix. Instead, localized LT application - for instance, printing a small label ($\sim$1–2 cm^2) on the surface of the item - is sufficient to produce a detectable signal in upgraded sorting systems. As shown in this study, the brightness of an LT is determined by the combined effects of PLQY and particle size, all of which must be jointly optimized.

Yb^{3+} is particularly well-suited as a sensitizer ion due to its strong absorption near 940–980 nm, and can be coupled with various activators (Er^{3+}, Ho^{3+}, Tm^{3+}, or Pr^{3+}) to yield LTs with unique spectral signatures in the SWIR region. Moreover, the same ion pairs - Yb^{3+}/Er^{3+}, Yb^{3+}/Ho^{3+}, and Yb^{3+}/Tm^{3+} - can be tuned *via* concentration and host matrix selection to produce upconversion luminescence, further expanding the number of distinguishable LT options to at least seven. Additionally, SWIR-emitting transition metal ions such as Ni^{2+}, Co^{3+}, and Fe^{3+} could also be explored to diversify the LT palette.

(2) High stability: chemical, thermal and photo stability are critical for real-world implementation. Oxide-based LTs, such as the YPO_4-based systems investigated here, generally can offer superior stability compared to halide or chalcogenide hosts. YPO_4 is particularly attractive due to its low solubility and resistance to hydrolysis, carbonation, and redox degradation.[50] For applications such as food-contact packaging, regulatory approval (*e.g.*, from the Food and Drug Administration (FDA) or European Food Safety Authority (EFSA) may be required). Notably, the commercial LT used as the reference in this study - $Y_2O_2S:Yb^{3+}/Er^{3+}$ - has already received such approval.

(3) Scalable and cost-effective production: LTs must be compatible with scalable manufacturing processes. For example, they must be synthesized with SSR as in the current work. In 2024, the global average per capita plastic waste generation was approximately 28 kg, whereas in Germany it was around 55 kg. Assuming an average packaging item mass of 30 g, this equates to $\sim$2000 items of plastic waste per person annually in Germany. To ensure reliable detection, the use of two printed labels per item is foreseen, each with a surface area of 1 cm^2 and an LT loading of 10 μg cm^{-2}. For a country like Germany (population $\sim$80 million), this would require approximately 3.2 metric tons of LT annually (based on YPO_4 formulations), corresponding to raw material demands of $\sim$1.2 tons Y_2O_3, $\sim$0.8 tons Yb_2O_3, and $\sim$0.08 tons Er_2O_3. Given current market prices (*e.g.*, $\sim$\$6000, $\sim$\$12 000, and $\sim$\$40 000 per ton for Y_2O_3, Yb_2O_3, and Er_2O_3,[51] respectively), the total material cost remains minimal, even under scenarios of large-scale implementation and when considering potential supply constraints.

The YPO_4-based LT developed and evaluated in this work serves as a model system illustrating how the integration of materials chemistry, spectroscopic characterization, and application-oriented design can lead to practical solutions for plastic labelling. The findings underscore the feasibility of deploying LT-based technologies on a large scale for plastic traceability, with potential to significantly improve sorting efficiency.

5. Conclusions

This work demonstrates that $YPO_4:Yb^{3+}/Er^{3+}$ phosphors with PLQY - up to 78% under 940 or 980 nm excitation (Yb^{3+}) and emission at 1540 nm (Er^{3+}) - can be synthesized using a flux-assisted SSR at 1100 °C for 12 h. The introduction of LiCl as a flux significantly reduces the synthesis temperature and time, enabling the preparation of comparable materials within 3 h at 900 °C, while maintaining high PLQY values. Although LiCl does not alter the YPO_4 crystal structure - neither by ionic substitution nor by occupying interstitial sites - its presence during synthesis promotes particle growth and improves Yb^{3+}/Er^{3+} intermixing. This enhanced mixing increases the energy-transfer efficiency from Yb^{3+} to Er^{3+} to 85%, which is a key factor responsible for the high PLQY achieved.

In realistic application formats, such as PDMS films or flexographically printed labels, PLQY alone does not determine the luminescence intensity (brightness) of the LT. Particle size distribution plays a crucial role in modulating both the excitation and emission through scattering effects. Notably, a commercial LT with a PLQY of only 7% outperformed the as-synthesized $YPO_4:Yb^{3+}/Er^{3+}$ sample (PLQY 78%) in terms of observed brightness, due to its more favourable particle size characteristics.

Mechanical milling of $YPO_4:Yb^{3+}/Er^{3+}$ resulted in reduced particle sizes and enhanced luminescence brightness, despite a moderate decrease in PLQY. In particular, milled YPO_4-based LTs outperformed the reference material when applied *via* industrially relevant printing methods, such as flexography, onto polyethylene substrates - a representative example of packaging materials.

These findings highlight the importance of balancing luminescence efficiency with physical parameters, such as particle size, to optimise LT performance in real-world applications. The results demonstrate the potential of LT-based plastic labelling as a valuable addition to existing near-infrared sorting systems, improving identification accuracy and enabling the classification of similar packaging. However, to realise this approach's full potential, continued development of LTs with unique spectral fingerprints will be essential.

Conflicts of interest

There are no conflicts to declare.

Data availability

Data are available on request from the corresponding authors.

Additional data supporting this article is included in the supplementary information (SI). Supplementary information is available. See DOI: https://doi.org/10.1039/d5ma01022e.

Acknowledgements

The financial support provided by the Helmholtz Association is gratefully acknowledged: (i) a Recruitment Initiative Fellowship for B. S. R.; and (ii) Research Field Energy – Program Materials and Technologies for the Energy Transition – Topic 1 Photovoltaics (38.01.02). B. S. R. and A. T. acknowledge funding from the European Union's Horizon 2020 research and innovation project "Circular Foodpack" agreement No: 101003806. The authors acknowledge Dr Andreas Kulawig and Dr Ralf Leineweber (Siegwerk Druckfarben AG & Co. KGaA) for their help in printing the PE pouch. L. J. B. E. would like to acknowledge the financial support provided by The World Academy of Sciences (TWAS) and the Deutsche Forschungsgemeinschaft (DFG) through their cooperation visits programme.

References

1 R. R. Larder and F. L. Hatton, *ACS Polym. Au*, 2022, **3**, 182–201.
2 M. Kumar, S. K. Bhujbal, K. Kohli, R. Prajapati, B. K. Sharma, A. D. Sawarkar, K. Abhishek, S. Bolan, P. Ghosh and M. Kirkham, *Sci. Total Environ.*, 2024, **921**, 171106.
3 L. Operato, A. Panzeri, G. Masoero, A. Gallo, L. Gomes and W. Hamd, *FFST*, 2025, **5**, 1520532.
4 T. Nguyen, J. Merna, E. Kysor, O. Kohlmann and D. B. Levin, *Polymers*, 2024, **16**, 2865.
5 Plastics – the fast Facts 2024, https://plasticseurope.org/knowledge-hub/plastics-the-fast-facts-2024/, (accessed 01.12.2025, 2025).
6 Packaging waste, https://environment.ec.europa.eu/topics/waste-and-recycling/packaging-waste_en, (accessed 01.12.2025, 2025).
7 EU Packaging and Packaging Waste Regulation, https://www.nnz.de/eu-packaging-and-packaging-waste-regulation-ppwr/#:~:text=Waste%20Reduction:By%202030%2C%20EU%20member%20states%20must,will%20need%20to%20be%20recycled%20at%20scale, (accessed 01.12.2025, 2025).
8 Regulation (EU) 2025/40 of the European Parliament, https://eur-lex.europa.eu/legal-content/EN/TXT/?uri=OJ:L_202500040&pk_campaign=todays_OJ&pk_source=EUR-Lex&pk_medium=X&pk_content=Environment&pk_keyword=Regulation, (accessed 01.12.2025).
9 I. A. Howard, D. Busko, G. Gao, P. Wendler, E. Madirov, A. Turshatov, J. Moesslein and B. S. Richards, *Resour., Conserv. Recycl.*, 2024, **205**, 107557.
10 C. Jehanno, J. W. Alty, M. Roosen, S. De Meester, A. P. Dove, E. Y.-X. Chen, F. A. Leibfarth and H. Sardon, *Nature*, 2022, **603**, 803–814.
11 P. Stegmann, V. Daioglou, M. Londo, D. P. van Vuuren and M. Junginger, *Nature*, 2022, **612**, 272–276.
12 J. Gasde, J. Woidasky, J. Moesslein and C. Lang-Koetz, *Sustainability*, 2020, **13**, 258.
13 Mechanical vs Chemical Recycling: An Introduction, https://www.richmondcontainers.com/b/mechanical-vs-chemical-recycling#:~:text=produce%20economic%20returns.-,Cons,form;%20not%20used%20as%20fuel, (accessed 01.12.2025).
14 Polymer Recycling Methods - AZO materials, https://www.azom.com/article.aspx?ArticleID=22798#:~:text=Pittcon%202023%20%2D%20Insights%20and%20Innovations,and%20quaternary%20recycling/energy%20recovery, (accessed 01.12.2025).
15 A. Cosgun Ergene, E. Madirov, E. Coetsee-Hugo, H. Swart, B. S. Richards and A. Turshatov, *Adv. Opt. Mater.*, 2024, **12**, 2400925.
16 S. R. Nicholson, J. E. Rorrer, A. Singh, M. O. Konev, N. A. Rorrer, A. C. Carpenter, A. J. Jacobsen, Y. Román-Leshkov and G. T. Beckham, *Annu. Rev. Chem. Biomol. Eng.*, 2022, **13**, 301–324.
17 M. Jakobs and N. Kroell, *Resour., Conserv. Recycl.*, 2024, **207**, 107599.
18 Tracer-Based-Sorting (TBS), https://www.hs-pforzheim.de/en/research/research_institutes/inec/projects/marek/tracer_based_sorting, (accessed 01.12.2025).
19 High Detection Rate - Tracer-based sorting (TBS) technology - Polysecure, https://www.polysecure.eu/en/sort-reliably/tracer-based-sorting, (accessed 01.12.2025, 2025).
20 FDA approval for markers in plastics with food contact, https://www.polysecure.eu/en/company/news#c1250, (accessed 01.12.2025).
21 K. Muthamma, B. Pallavi, D. Sunil, S. D. Kulkarni, S. Wagle and D. Kekuda, *Colloids Surf., A*, 2022, **653**, 129910.
22 J.-H. Song, J. Kim, H. Jang, I. Yong Kim, I. Karnadi, J. Shin, J. H. Shin and Y.-H. Lee, *Nat. Commun.*, 2015, **6**, 7080.
23 E. Paradisi, C. Mortalò, V. Zin, F. Armetta, V. Boiko, D. Hreniak, M. Zapparoli, S. M. Deambrosis, E. Miorin and C. Leonelli, *ACS Appl. Nano Mater.*, 2024, **7**, 6893–6905.
24 L. Yang, B. Teng, D. Zhong, W. Han, J. He, Y. Xu, M. Zhu, J. Tang, S. Ji and J. Liu, *Opt. Mater. Express*, 2017, **7**, 3618–3625.
25 J. Nedelec, D. Avignant and R. Mahiou, *Chem. Mater.*, 2002, **14**, 651–655.
26 F. Armetta, V. Boiko, D. Hreniak, C. Mortalò, C. Leonelli, L. Barbata and M. L. Saladino, *Ceram. Int.*, 2023, **49**, 23287–23294.
27 N. Bhiri, H. Duim, E. Madirov, J. Nyarige, B. S. Richards and A. Turshatov, *J. Mater. Chem. C*, 2025, **13**, 4605–4615.
28 O. Lehmann, H. Meyssamy, K. Kömpe, H. Schnablegger and M. Haase, *J. Phys. Chem. B*, 2003, **107**, 7449–7453.
29 Y. Che, S. Sun, J. Lu, F. Zheng, G. Yu, Y. Cao, L. Wang, L. Sun, Y. Yin and Z. Wang, *J. Lumin.*, 2022, **248**, 118957.
30 H. Won, H. Nersisyan, C. Won and K. Lee, *Mater. Chem. Phys.*, 2011, **129**, 955–960.
31 Y.-K. Su, Y.-M. Peng, R.-Y. Yang and J.-L. Chen, *Opt. Mater.*, 2012, **34**, 1598–1602.
32 L. Liu, R.-J. Xie, C. Zhang and N. Hirosaki, *Materials*, 2013, **6**, 2862–2872.
33 D. Dhaterwal, M. Matoria and S. Singh, *Next Nanotechnol.*, 2024, 100033.
34 M. Hu, C. Liao, L. Xia, W. You and Z. Li, *J. Lumin.*, 2019, **211**, 114–120.
35 N. Zhang, Z. Wang, H. Zhang, Y. Sun, T. Yuan, C. Tao, Z. Yang and P. Li, *Ceram. Int.*, 2019, **45**, 18876–18886.
36 Y.-P. Lan, C. Chen, J. Li, X. Xia, X. Mao and H. Zhou, *Ceram. Int.*, 2021, **47**, 4793–4802.

37 K.-L. Wong, J.-C. G. Bünzli and P. A. Tanner, *J. Lumin.*, 2020, **224**, 117256.
38 K. Momma and F. Izumi, *J. Appl. Crystallogr.*, 2011, **44**, 1272–1276.
39 S. Leyre, E. Coutino-Gonzalez, J. Joos, J. Ryckaert, Y. Meuret, D. Poelman, P. Smet, G. Durinck, J. Hofkens and G. Deconinck, *Rev. Sci. Instrum.*, 2014, **85**, 123115.
40 L. R. Wilson and B. S. Richards, *Appl. Opt.*, 2009, **48**, 212–220.
41 Z. Yahiaoui, M. Hassairi and M. Dammak, *J. Electron. Mater.*, 2017, **46**, 4765–4773.
42 R. E. Joseph, D. Busko, D. Hudry, G. Gao, D. Biner, K. Krämer, A. Turshatov, B. S. Richards and I. A. Howard, *Opt. Mater.*, 2018, **82**, 65–70.
43 M.-J. Sánchez-Rivera, M. J. Orts, V. Pérez-Herranz and S. Mestre, *BSECV*, 2023, **62**, 194–202.
44 A. R. Kamali, D. J. Fray and C. Schwandt, *J. Therm. Anal. Calorim.*, 2011, **104**, 619–626.
45 C. Olscher, A. Jandric, C. Zafiu and F. Part, *Polymers*, 2022, **14**, 3074.
46 G. Cai, L. Giordano, C. Richard and B. Viana, *Nanomaterials*, 2023, **13**, 2175.
47 V. Havasi, D. Tátrai, G. Szabó, E. Varga, A. Erdőhelyi, G. Sipos, Z. Kónya and Á. Kukovecz, *J. Lumin.*, 2020, **219**, 116917.
48 N.-K. Yu, L. F. Rasteiro, V. S. Nguyen, K. M. Golabek, C. Sievers and A. J. Medford, *JACS Au*, 2024, **5**, 82–90.
49 L. N. Elliott, D. Austin, R. A. Bourne, A. Hassanpour, J. Robb, J. L. Edwards, S. Sutcliffe and T. N. Hunter, *Langmuir*, 2023, **39**, 5697–5709.
50 Y. Wang, X. Chen, W. Liu, L. Cheng and L. Zhang, *Ceram. Int.*, 2010, **36**, 755–759.
51 Rare Earth Oxides prices, https://www.metal.com/price/Rare-Earth/Rare-Earth-Oxides (accessed 01.12.2025, 2025).